Canalization of circuit assembly by δ-protocadherins in the zebrafish optic tectum

Sayantanee Biswas[1], Michelle R. Emond[1], Grace S. Philip[1] and James D. Jontes[1,*]

[1]Department of Biological Chemistry and Pharmacology
Ohio State University Wexner College of Medicine
Columbus, OH 43210

*corresponding author: jontes.1@osu.edu

Abstract

Neurons are precisely and reproducibly assembled into complex networks during development. How genes collaborate to guide this assembly remains an enduring mystery. In humans, large numbers of genes have been implicated in neurodevelopmental disorders that are characterized by variable and overlapping phenotypes. The complexity of the brain, the large number of genes involved and the heterogeneity of the disorders makes understanding the relationships between genes, development and neural function challenging. Waddington suggested the concept of canalization to describe the role of genes in shaping developmental trajectories that lead to precise outcomes[1] . Here, we show that members of the δ-protocadherin family of homophilic adhesion molecules, Protocadherin-19 and Protocadherin-17, contribute to developmental canalization of visual circuit assembly in the zebrafish. We provided oriented visual stimuli to zebrafish larvae and performed *in vivo* 2-photon calcium imaging in the optic tectum. The latent dynamics resulting from the population activity were confined to a conserved manifold. Among different wild type larvae, these dynamics were remarkably similar, allowing quantitative comparisons within and among genotypes. In both Protocadherin-19 and Protocadherin-17 mutants, the latent dynamics diverged from wild type. Importantly, these deviations could be averaged away, suggesting that the loss of these adhesion molecules leads to stochastic phenotypic variability and introduced disruptions of circuit organization that varied among individual mutants. These results provide a specific, quantitative example of canalization in the development of a vertebrate neural circuit, and suggest a framework for understanding the observed variability in complex brain disorders.

33 ***Introduction***

34 Despite their immense complexity, vertebrate brains are highly organized and exhibit a
35 conserved, stereotyped architecture. Distinct brain regions comprise canonical circuits that carry out
36 well-defined functions, which are conserved both within and between species[2,3] . The assembly of these
37 conserved circuits is robust to genetic and environmental variation, as well as natural biological
38 heterogeneity. This allows the brains of distinct individuals to perform the same tasks, even though they
39 are not identical at the level of neurons and synapses, or in their particular developmental histories. The
40 mechanisms that confer robust circuit development in the face of these multiple sources of variability are
41 poorly understood[4,5] .

42 In the case of neurodevelopmental disorders, such as schizophrenia and autism, the relationship
43 between conserved structure and conserved function breaks down. Characterized by profound
44 disturbances in normal brain function, some evidence suggests that these disorders are
45 "connectopathies," arising from disruption of the underlying network topology[6–10] . While a large number
46 of genes have been linked to developmental brain disorders, understanding the relationship of genotype
47 to phenotype is challenging. In addition to natural biological variability, these disorders are plagued by
48 variability in penetrance and expressivity[11,12] . Moreover, putatively distinct disorders have amorphous
49 boundaries, overlapping with one another and exhibiting comorbidities[13], as well as sharing genetic
50 origins[14–16] . Collectively, these sources of variation mask the relationships between gene function,
51 circuit organization and neural activity. These same issues make interpretation of studies in animal
52 models similarly challenging.

53 Protocadherin-19 is a member of the δ-protocadherin family of homophilic cell adhesion
54 molecules[17–19] . In humans, mutations in *PCDH19* are linked to schizophrenia and autism[20,21] , and cause
55 a developmental epileptic encephalopathy[22,23]. To investigate how mutations in *pcdh19* or the related
56 *pcdh17* affect neural development, we used visual stimulation and *in vivo* 2-photon calcium imaging in
57 the optic tectum of the larval zebrafish. We show that the neuronal population responses to oriented
58 sinusoidal gratings define neural dynamics that are strongly stereotyped among wild type larvae. In
59 mutants, these dynamics are altered, reflecting stochastic deviations in circuit organization. Our results

are consistent with a role for protocadherins in canalization of development, contributing to robustness of circuit assembly. This can provide a conceptual framework for understanding the variability associated with neurodevelopmental disorders.

Results

Moving stimuli, such as moving lines, spots or gratings, elicit robust responses in the optic tectum of zebrafish[24–27]. To record the activity of tectal neurons, we generated a transgenic line that *pan*-neuronally expresses a nuclear localized jGCaMP8s (Histone H2B-GCaMP8s). These transgenic larvae were mounted in a custom imaging chamber **(Fig. 1a**), and we elicited visual responses by projecting a sequence of drifting sinusoidal gratings (12 directions rotated at 30º intervals) onto an adjacent translucent screen (**Fig. 1b,c**). Two-photon image stacks spanning the optic tectum (7 optical sections at 10 µm spacing) were collected at 1 Hz (**Fig. 1d**), allowing us to sample population activity. We used constrained non-negative matrix factorization (CNMF) with CaImAn[28] to automatically segment images and extract fluorescence traces from visually-responsive neurons (**Fig. 1e,f**). For further analysis, the neural responses were averaged across three trials (**Fig. 1g**). Overall, we obtained 2506 visually responsive neurons (n=9).

It is now widely understood that sensory processing and motor control are encoded by neuronal population dynamics, rather than the activities of individual neurons[29,30] . These latent dynamics consist of a small number of covariation patterns, or neural modes, which describe a neural manifold within a low-dimensional subspace[31–33] . To explore the structure of tectal population dynamics in response to visual stimulation, we performed linear dimensionality reduction with principal component analysis (PCA) (**Fig. 2a**). For n neurons, PCA reduces the data from an n-dimensional space to a more compact k-dimensional space. We found that the first five neural modes captured 89.9±1.8% (n=9; mean ± sem.) of the variance in our wild type data (**Fig. 2b**), and our subsequent analyses are confined to these five neural modes. Each axis represents a significant pattern of neuronal covariation that is activated to varying extent during the presentation of visual stimuli, and projection of the original neural data onto these axes describes the latent dynamics evoked by visual stimulation (**Fig. 2c**). To determine how

87 consistent the neural responses are in individual larvae, the latent dynamics were obtained for individual
88 trials, and the Pearson's correlation (r) between individual trials was calculated along each dimension
89 (**Fig. 2c,d**). The mean trial-to-trial correlation was greater than 0.9 across all 5 neural modes (**Fig. 2d**).
90 Recent evidence suggests that the similarity of neural architecture among individuals gives rise to similar
91 latent dynamics for a given stimulus or motor task[34] . In mammals, latent dynamics are estimated from a
92 small subsample of neurons, which varies from individual to individual. In such cases, the latent
93 dynamics from different animals need to be aligned using a procedure such as canonical correlation
94 analysis[34,35] . Here, we image a relatively large proportion of visually-responsive neurons and sample
95 among the same neuronal types across different fish, obviating the need for alignment. For each wild
96 type individual, we determined the latent dynamics from trial averaged responses (**Fig. 2e**). To quantify
97 the similarity of the dynamics among the pool of wild types, we generated the averaged response, then
98 calculated Pearson's correlation between this average and the dynamics of each individual (**Fig. 2e,f**).
99 The mean correlation along each neural mode was nearly as high as for trial-to-trial correlations (**Fig.
100 2c,d**), indicating that the similarity of dynamics among individuals is comparable to the similarity of
101 successive trials in the same individual. Thus, the latent dynamics elicited by visual stimulation is
102 stereotyped across different zebrafish larvae, facilitating comparisons within and among experimental
103 groups. While the latent dynamics among wild type larvae are strongly correlated, it is possible that the
104 correlation could be improved by further alignment. To test this, we performed Canonical Correlation
105 Analysis (CCA) on our wild type datasets, but found that alignment degraded the correlation of dynamics
106 derived from wild type larvae (*not shown*). When plotted in three dimensions, the latent dynamics from
107 individual larvae describe a rosette shaped trajectory, with each leaf representing the response to a
108 direction of grating drift (**Fig. 2g,h**). The averaged dynamics yielded a smooth trajectory in three
109 dimensions (**Fig. 2i**). Thus, the population response to our simple stimulus presentation, encodes the
110 direction of motion on a neural manifold that is preserved across zebrafish larvae.

111 To investigate the involvement of *pcdh19* in the assembly of visual circuitry we used two, distinct
112 *pcdh19* mutant alleles. We previously introduced an indel lesion near the 5' end of exon1 shortly after
113 the sequence encoding the signal peptide[36,37] , resulting in a complete lack of functional Pcdh19 (*pcdh19*$^{-}$

114 ^{10bp}). In addition, we have generated a new "promoterless" *pcdh19* allele, which lacks ~4kb of genomic
115 sequence, spanning the basal promoter, 5'UTR and the ATG start codon in exon 1 (*pcdh19*$^{\Delta prom}$)(**Fig.**
116 **S1a,b**). While both alleles completely eliminate the production of Pcdh19 protein (**Fig. S1c**), evidence
117 suggests that indel mutations, like *pcdh19*$^{-10bp}$, can elicit compensatory mechanisms arising from
118 nonsense-mediated RNA decay[38,39] . Both of these mutant lines were crossed into our *Tg(elav3l:H2B-*
119 *GCaMP8s)* line. As above, we performed calcium imaging on homozygous mutants during visual
120 stimulation, and computed the latent dynamics for each mutant from the trial averages of visually
121 responsive neurons (**Fig. 3a,b**). To determine whether the mutant groups differed from wild type in their
122 visual responses, we correlated the trial-averaged dynamics from each individual mutant with the wild
123 type group average along each neural mode (**Fig. 3c**). Both *pcdh19*$^{-10bp}$ and *pcdh19*$^{\Delta prom}$ showed
124 decreased correlation with the group average (**Fig. 3c**), although this varied by neural mode between the
125 two mutants. The *pcdh19*$^{-10bp}$ larvae showed the greatest change along the second neural mode, while
126 *pcdh19*$^{\Delta prom}$ mutants exhibited significant differences along neural modes 2-5 (**Fig. 3c**). The response to
127 drifting sinusoidal gratings diverged from wild type for both *pcdh19* mutants, as the trajectories of
128 individual mutant fish were less correlated to the wild type average than were individual wild type fish. To
129 determine whether individual mutants described similar or distinct trajectories, we calculated pairwise
130 correlations between larvae within an experimental group. If mutants converged on a distinct, but
131 stereotyped, circuit organization, then their intra-group correlation should be similar to the intra-group
132 correlations of the wild type group. Alternatively, if the divergence of the mutants from wild type is due to
133 stochastic variations, then the intra-group correlations should be lower and exhibit an increased variance.
134 Consistent with stochastic variation, the *pcdh19* mutants exhibit lower intra-group correlations than wild
135 type larvae (**Fig. 3d**). When visualized in three dimensions, the trajectories from individual *pcdh19*$^{\Delta prom}$
136 mutants differ dramatically from the stereotyped paths of wild type larvae (**Fig. 2g,h**), and diverge from
137 each other (**Fig. 3e,f**). However, despite the variability of the individual mutants, averaging within a
138 genotype suppresses this variation and gives rise to averaged dynamics that are strongly correlated with
139 wild type (**Fig. 3g**). This suggests that the effect of *pcdh19* loss on visual processing is best understood
140 as stochastic developmental noise, as this noise can be suppressed by averaging (**Fig. 3g**).

141 Pcdh19 is a member of a small family of related δ2-pcdhs. To determine if mutations in other δ2-
142 pcdhs also affect visual responses in the optic tectum, we recorded the response to visual stimulation in
143 mutants lacking *pcdh17* (*pcdh17*$^{-5bp}$)[37] . As above, we used the trial averaged neuronal responses to
144 compute the latent dynamics along the first five neural modes (**Fig. 4a**). Similar to the *pcdh19* mutants,
145 the latent dynamics exhibited by *pcdh17*$^{-5bp}$ mutants was less correlated with the wild type average (**Fig.**
146 **4a**), although the differences were not statistically significant (**Fig. 4b**). To measure the intra-group
147 variation exhibited by the *pcdh17*$^{-5bp}$ mutants, we determined pairwise correlations along each neural
148 mode (**Fig. 4c**). Although there was a uniform decrease in pairwise correlation among the *pcdh17*$^{-5bp}$
149 mutants, this was only significant for neural mode 5 (**Fig. 4c**). This observed intra-group noise was
150 eliminated by averaging, as the *pcdh17*$^{-5bp}$ group average exhibited high correlation with the wild type
151 average (**Fig 4d**). As each mutant genotype showed a reduced intra-group correlation, it is possible that
152 this increased variation is due to unreliable or noisy neuronal responses. To determine whether the
153 tectal responses to visual stimulation are reliable, we determined the between-trial correlations for each
154 neural mode within each experimental group (**Fig. 4e**). We found no significant difference in the
155 between-trial consistency of the population dynamics in the mutant groups, compared to wild type (**Fig.**
156 **4e**). This suggests that each mutant network is responding reliably and reproducibly to repeated
157 presentations of a given stimulus, yet deviates randomly from the wild type. To quantify the within-group
158 variance, we generated histograms of all pairwise correlation coefficients within each experimental group
159 (**Fig. 4f**). While the distribution of correlation coefficients for the wild type group is narrow and
160 concentrated at higher correlations, the mutants all exhibit significantly broader distributions (**Fig. 4f**). To
161 provide a metric for the overall similarity of latent dynamics among different larvae, we calculated the
162 mean r of individual correlations across the five neural modes for each genotype (**Fig. 4g**). If the
163 computed dynamics are empirical estimates of the neural manifold, then this summary r should measure
164 the similarity of an individual manifold to the averaged wild type manifold. In the case of each mutant
165 genotype, the dynamics are significantly different from wild type, although the effect is more robust for
166 the *pcdh19*$^{\Delta prom}$ mutants (**Fig. 4g**). While the variations along individual neural modes are not considered
167 to be statistically significant for the *pcdh17*$^{-5bp}$ mutants, the aggregate impact on the shape of the neural

168 manifold is significant (**Fig. 4g**). Thus, loss of either *pcdh19* or *pcdh17* alters the neural population
169 response to visual stimulation, by introducing stochastic perturbations into circuit assembly. Our data are
170 consistent with the idea that δ2-pcdhs contribute to canalization of the developing optic tectum (**Fig. 4h**).
171 To determine the relationship of the altered latent dynamics in the pcdh mutants to more traditional
172 measures of neuronal responses, we determined the orientation and direction selectivity for neurons in
173 wild type larvae and each of the mutants (**Fig. S2**). For each neuron, we determined an orientation
174 selectivity index (OSI), direction selectivity index (DSI) and preferred direction. The the *pcdh17*$^{-5bp}$
175 mutants exhibited a dramatic decrease in orientation selectivity (**Fig. S2a**) and direction selectivity (**Fig.**
176 **S2b**), while both *pcdh19*$^{-10bp}$ and *pcdh19*$^{\Delta prom}$ showed a shift toward increased orientation selectivity and
177 a modest decrease in direction selectivity in the *pcdh19*$^{\Delta prom}$ mutants. The distribution of preferred
178 orientations also exhibited differences among the mutants, as *pcdh17*$^{-5bp}$ mutants exhibited a decreased
179 response to rostral-to-caudal motion (**Fig. S2c,d**), and both *pcdh19*$^{-10bp}$ (**Fig. S2c,e**) and *pcdh19*$^{\Delta prom}$
180 (**Fig. S3c,f**) showed an increase in the proportion of neurons responding to rostral-to-caudal motion.
181 In addition to homozygous mutants, we also analyzed the visual responses of heterozygous
182 mutants (**Fig. S3**). Latent dynamics in the heterozygotes was similar to each of the respective
183 homozygous mutants (**Fig. S3a-c**). Both the correlation of individual neural modes to the wild type
184 average (**Fig. S3d**) and the pairwise, within-group correlations (**Fig. S3e**) were lower than for wild type
185 and the reduction was comparable in magnitude to what we observed in homozygous mutants. When
186 averaged across neural modes, the mean similarity of each δ2-pcdh mutant to the wild type neural
187 response was reduced (**Fig. S3f**), and was characterized by increased within-group variation (**Fig. S3g**).
188 As was observed for homozygous mutants (**Fig. 3,4**), this variability could be averaged away and
189 averages of the heterozygous mutants were highly correlated with the wild type average (**Fig. S3h,i**).
190

191 ***Discussion***

192 The δ2-pcdhs comprise a subfamily of homophilic cell adhesion molecules within the cadherin
193 superfamily, and are associated with neurodevelopmental disorders in humans[40,41] . Among the five δ2-
194 pcdhs in mammals, all are linked to human disorders: *PCDH8* and *PCDH10* are linked to autism[42,43] , a

genomic deletion encompassing *PCDH18* caused severe intellectual disability[44] , *PCDH17* is implicated in mood disorders[45] , and mutations in *PCDH19* cause a developmental epileptic encephalopathy[22,23] , and are associated with autism and schizophrenia [20,21] . We previously used large-scale *in vivo* calcium imaging of spontaneous activity and network analysis to show that zebrafish mutants lacking *pcdh19* had defects in network topology[46] . Subsequently, others showed that mutant rodents and zebrafish larvae were hyperexcitable[47,48] , and that mutant rodents showed increased network synchrony[47] . Here, our results show that loss of either *pcdh19* or *pcdh17* impairs visual processing in the optic tectum of the larval zebrafish.

Our data show that the response of the larval optic tectum to moving sinusoidal gratings is encoded by low-dimensional dynamics that are confined to a neural manifold. These dynamics are highly stereotyped among wild type individuals. It was recently shown that dynamics are preserved across individuals within a species, but these dynamics need to be aligned using a procedure such as canonical correlation analysis[34], due to the fact that the latent dynamics are estimated from only a small subsample of neurons that vary among animals. Here, we image a substantial proportion of the visually responsive neurons in the optic tectum. Consequently, the dynamics derived from different individuals do not require further alignment. This allows the complex neural responses of hundreds of neurons in different animals to be reduced to a common set of activity patterns that can be quantitatively compared within and between genotypes. The variation among wild type individual larvae is very low, indicating that development within a population gives rise to an ensemble of equivalent networks that differ in the precise number, morphology and connectivity of the constituent neurons, but whose overall functional variation is low.

Elimination of either *pcdh19* or *pcdh17* leads to altered latent dynamics. The stereotyped neural response that characterizes the population of wild type larvae is degraded in the mutants, whose dynamics are less well correlated to the averaged wild type response. The latent dynamics among the mutant genotypes varies by individual. As a consequence, within a mutant group, individuals are much less similar to each other than the pool of wild type larvae are to each other. Additionally, this stochastic variability is masked in a group average, as the deviations specific to an individual can be averaged

222 away. This implies that the loss of Pcdh19 or Pcdh17 does not lead to a particular, alternative network
223 structure, but to a stochastic array of alternatives. Thus, the effects of the *pcdh19* and *pcdh17* mutations
224 are best understood as an increase in developmental noise, leading to an increase in phenotypic
225 variability. Our data show that the effects of a well-defined genetic lesion on a simple, highly stereotyped
226 network can be stochastic. While both *pcdh19*$^{-10bp}$ and *pcdh19*$^{\Delta prom}$ mutants result in a complete loss of
227 Pcdh19 protein, their effects on the optic tectum are not identical. The phenotype associated with
228 Pcdh19 loss in the *pcdh19*$^{\Delta prom}$ line is significantly more severe than in the *pcdh19*$^{-10bp}$ line. Combined
229 with the observation that the magnitude of the impact of indel mutations in *pcdh19*$^{-10bp}$ and *pcdh17*$^{-5bp}$ is
230 similar, this suggests that the difference could be due to the activation of compensatory mechanisms by
231 the indel mutations that are absent in the promoterless allele. This may indicate a further source of
232 variability in understanding neural disorders and in the study of relevant genes in animal models, as even
233 alternative "null" mutations may give rise to distinct phenotypes.
234 In evolution, strong selective pressures prevent the accumulation of mutations that have an
235 adverse impact on phenotypic fitness. Release of a selective pressure can then lead to an increase in
236 allelic and phenotypic diversity within a population. By analogy, our results suggest that Pcdh19 and
237 Pcdh17 suppress variation in the development of tectal circuitry. Loss of either protocadherin releases a
238 constraint on circuit assembly, allowing stochastic variation in circuit organization and function. These
239 results suggest that Pcdh19 and Pcdh17 contribute to developmental robustness by canalizing circuit
240 assembly and limiting developmental variability. While canalization is most commonly discussed in terms
241 of gene regulatory networks buffering against adverse genetic or environmental effects[49,50] , we suggest
242 that the protocadherins may buffer against the formation of inappropriate connections and help guide
243 circuit assembly toward an optimal outcome. These results suggest that while the heterogeneity
244 observed in neurodevelopmental disorders is often attributed to polygenic effects, it could also be due to
245 decanalization of circuit assembly and stochastic degradation of circuit function.
246
247 ***Methods***
248 *Zebrafish maintenance and generation of lines*

249 Adult zebrafish (Danio rerio) were maintained at ~28.5°C and staged according to Westerfield
250 (1995). All animal procedures were performed in accordance with the Ohio State University animal care
251 committee's regulations. We previously generated lines harboring germline mutations of *pcdh19*
252 (*pcdh19*^{os51})[36] and *pcdh17* (*pcdh17*^{os69})[37] .
253 The *pcdh19*$^{\Delta prom}$ mutant line (*pcdh19*^{os77}) was established by co-injecting ribonucleoprotein
254 complexes (Integrated DNA Technologies) consisting of Cas9 protein and gRNAs targeting a site in the
255 5' end of *pcdh19* exon1 (GGGCTCAGATTAACCCATCG) and ~4 kb upstream of the ATG start codon
256 (CTGTTGTGAGCTAGTTACCA), which is predicted to eliminate the promoter region. Founders were
257 identified by PCR and sequenced, confirming the large genomic deletion. Like the *pcdh19*$^{-10bp}$ line,
258 Western blots confirmed that the homozygous *pcdh19*$^{\Delta prom}$ line produced no Pcdh19 protein.
259 The plasmid *Tol2-elavl3:H2B-GCaMP8s* was assembled using the following plasmids: Tol2-
260 elavl3-GCaMP6s (a gift from Misha Ahrens; Addgene plasmid # 59530 ; http://n2t.net/addgene:59530 ;
261 RRID:Addgene_59530), CMV:Histone H2B-mGL (H2B-mGreenLantern was a gift from Gregory Petsko;
262 Addgene plasmid # 164464 ; http://n2t.net/addgene:164464 ; RRID:Addgene_164464), and
263 CMV:jGCaMP8s (gift from GENIE Project; Addgene plasmid # 162371 ; http://n2t.net/addgene:162371 ;
264 RRID:Addgene_162371). Along with mRNA encoding Tol2 transpose, this plasmid was co-injected into
265 1 cell stage *nacre* embryos in order to establish the transgenic line *Tg(elavl3:H2B-GCaMP)*^{os78}. This
266 transgenic line was crossed with the *pcdh19*$^{-10bp}$, *pcdh19*$^{\Delta prom}$and *pcdh17*$^{-5bp}$ mutant lines.
267
268 *Calcium imaging*
269 Unanaesthetized 6 days-post-fertilization (dpf) larvae were embedded dorsal side up in 2% low
270 melting point agarose. Imaging was performed on a custom-built resonant-scanning 2-photon
271 microscope. Briefly, 920nm excitation was provided by an Axon920-TPC laser (Coherent, Inc.). We
272 used a Nikon Apochromat 25x/1.1NA water-immersion objective for imaging. The resonant scan-head
273 and controller, 3DMS robotic stage, Hamamatsu GaAsP photomultiplier tubes and power supply were
274 obtained from Sutter Instruments (www.sutter.com). A piezo-electric objective positioner (nPFocus250)

275 was obtained from nPoint (www.npoint.com). The microscope was run with ScanImage 5.2[51] (Vidrio
276 Technologies). All other parts were obtained from Thorlabs (www.thorlabs.com). Image stacks of 7
277 optical sections (512x512), spaced at 10 μm, were collected at 1 s intervals, with a pixel size of 0.65 μm.
278 For each group, we included data from 9-13 larvae, which is in line with the number of fish used in
279 comparable studies[52–54] . These were derived from at least two, separate crosses.
280
281 *Visual stimulation*
282 Visual stimuli were programmed in Python, using PsychoPy3 (https://psychopy.org). Moving sinusoidal
283 gratings were presented for 5 seconds, with 10 seconds of a neutral gray background in between each
284 direction, which were rotated at 30° intervals. The stimulus set was presented three times, with 50
285 seconds in between each presentation. Stimuli were projected onto a translucent screen 2.5 cm from the
286 larvae using a Rif6 cube picoprojector (rif6.com). The stimulus occupied ~104° of the visual field.
287
288 *Data analysis*
289 We used CaImAn-MATLAB for processing of calcium imaging movies[28] , including non-rigid
290 motion correction with NoRMCorre[55] . First, sequences of image stacks (735 stacks of 7 planes) were
291 re-formatted to movies of image planes (7 stacks of 735 timepoints). These were motion corrected and
292 inspected for motion artifacts. Movies that exhibited z-drift or other defects were discarded. Brightness
293 and contrast were adjusted and then images were masked in order to analyze only the left (visually-
294 responsive) hemi-tectum. CaImAn was used to segment movies and extract ΔF/F fluorescence traces.
295 Cells that were responsive to the visual stimuli in each of the three trials were selected for further
296 analysis.
297 Principal Component Analysis was performed on individual datasets. As ~90% of the variance
298 was explained by the top 5 principal components (neural modes), we restricted our analysis to these.
299 We projected the original neural responses onto these new basis vectors. The order of neural modes
300 varied among datasets, as did the sign of the neural mode. We established a standard order and
301 inspected each dataset to ensure a common order and sign for the neural modes. For comparisons of

neural modes among datasets, we used Pearson's correlation, r[34,35] . First, we averaged dynamics along each neural mode to generate a wild type average. Correlation of neural modes from individual larvae to the averaged neural modes provided a measure of variation. As an alternative measure of the variation in the datasets, each individual set of neural modes was correlated to all others within a group. This pairwise correlation describes how much latent dynamics varied among individuals within a genotype. To generate a single measure of similarity of latent dynamics between an individual and the wild type average, we averaged the correlation coefficients across the 5 neural modes. For comparisons, statistical significance was determined using Dunnett's test. For the comparison of distributions of r, we used a Dunn's test. To compare circular distributions, we used a MATLAB implementation of Watson's U^2 test (Pierre Mégevand (2025) pierremegevand/watsons_u2 https://github.com/pierremegevand/watsons_u2). All other statistical analysis was performed in JMP Pro 17.

Canonical Correlation Analysis

CCA was implemented in MATLAB and performed as described in Gallego et al. (2018). Briefly, a QR decomposition was performed on each set of dynamics to be aligned ($L_1 = Q_1R_1$ and $L_2 = Q_2R_2$), then a singular value decomposition was performed on the inner product of Q_1 and Q_2 ($USV^T = Q_1^TQ_2$). The dynamics were then aligned by $L_2' = L_2M_2M_1^{-1}$, where $M_1 = R_1^{-1}U$ and $M_2 = R_2^{-1}V$.

Acknowledgements

The content is solely the responsibility of the authors and does not necessarily represent the official views of the National Institutes of Health. Research reported in this publication was supported by the National Eye Institute of the National Institutes of Health under award number R21EY034706 and by the National Insitute of General Medical Sciences of the National Institutes of Health under award R01GM141280 to JDJ. We would like to thank Marcus Nichols for support with zebrafish maintenance and husbandry.

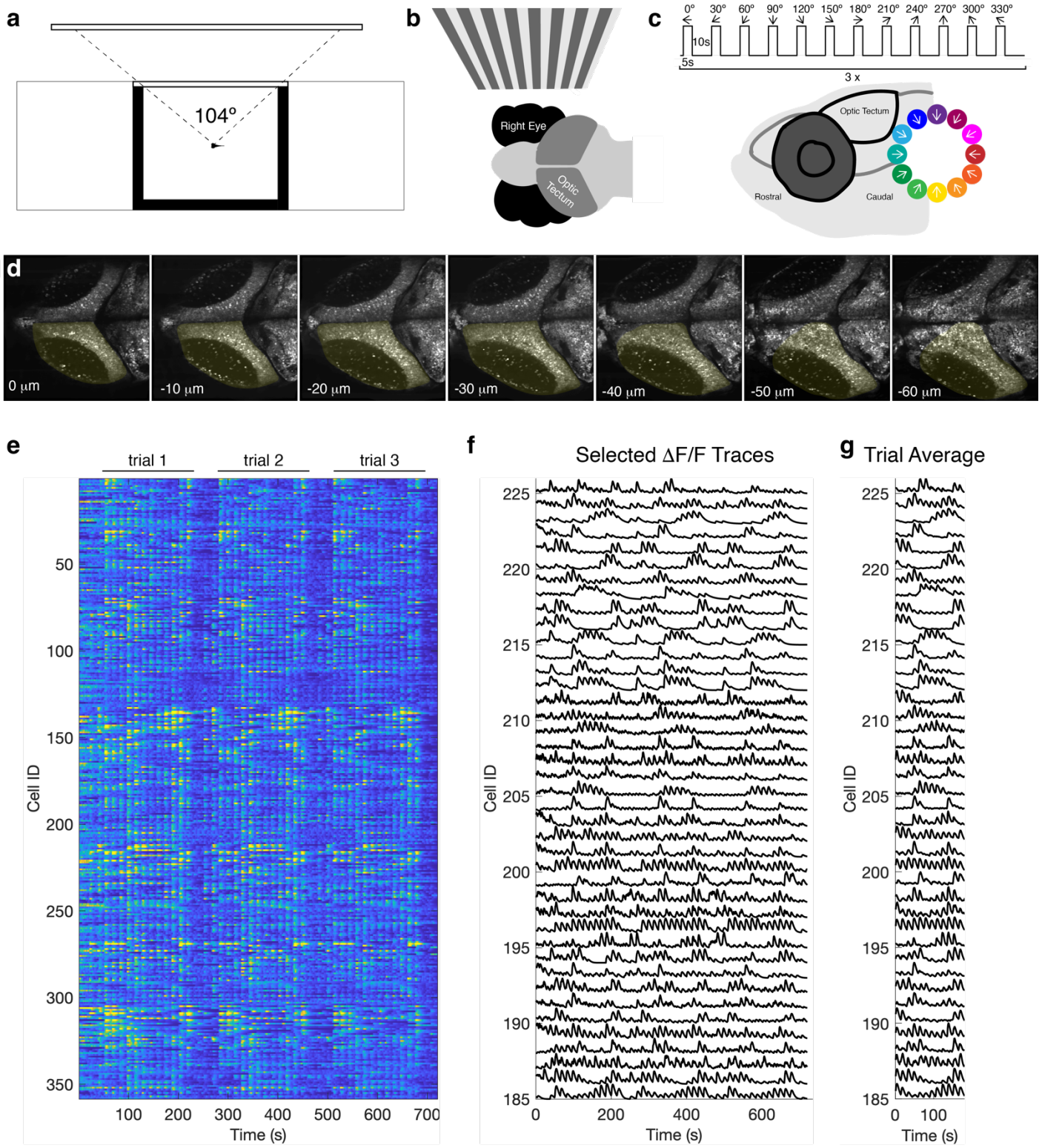

Figure 1. Calcium-imaging of neural responses to oriented sinusoidal gratings.
a. *Schematic of the experimental setup. A 6dpf larva is embedded in agarose in an imaging chamber, allowing 104º view of a projection screen.*
b. *The visual stimuli are presented to the right eye and the neural responses are visualized in the contralateral (left) hemi-tectum.*

c. *The stimulation protocol is a series of 5s on 10s off of a moving sinusoidal grating, 12 directions spaced at 30º intervals to encompass the full 360º. This is repeated three times. Below is a lateral view of the head of a zebrafish larva. The inset shows the directions of motion of sinusoidal gratings with reference to the rostro-caudal axis of the fish. The direction color-code is used throughout the paper.*
d. *Image stacks consisting of 7 optical sections spaced at 10 µm were collected at 1s intervals. Shown are average intensity images of individual planes from a timelapse sequence collected in a 6 dpf transgenic larva, Tg(elav3l:HistoneH2B-GCaMP8s). The visually-responsive hemi-tectum is outlined in yellow.*
e. *Example data showing all the fluorescence traces from visually-responsive neurons collected from one larva.*
f. *$\Delta F/F$ traces selected from those shown in* ***e****.*
g. *Responses were averaged across the three trials. Shown are the trial averages from the traces in* ***f****.*

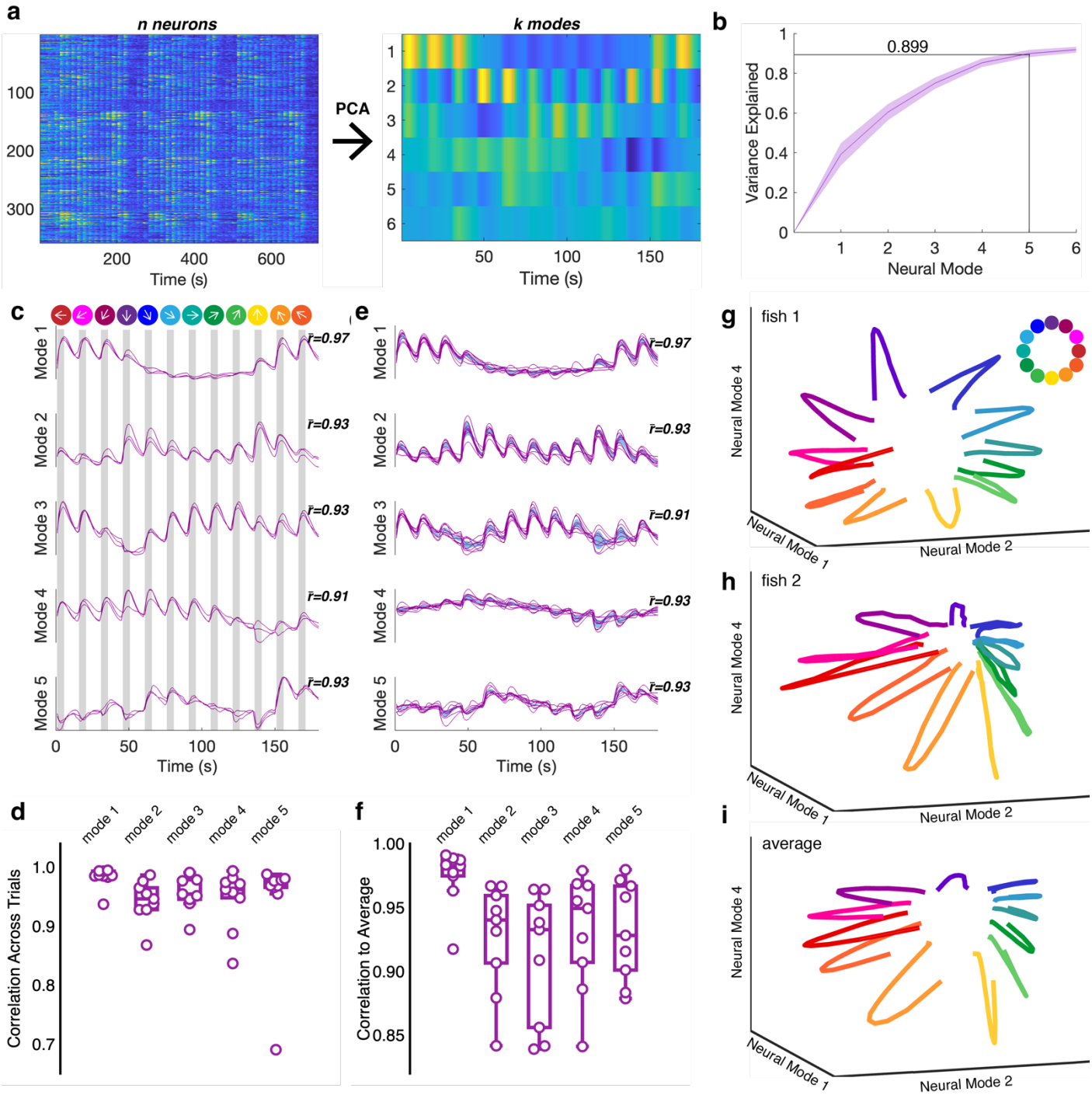
a
n neurons
100
200
300
200
400
600
Time (s)
PCA
k modes
1
2
3
4
5
6
50
100
150
Time (s)
b
0.899
Variance Explained
Neural Mode
c
Mode 1
Mode 2
Mode 3
Mode 4
Mode 5
r̄=0.97
r̄=0.93
r̄=0.93
r̄=0.91
r̄=0.93
Time (s)
e
r̄=0.97
r̄=0.93
r̄=0.91
r̄=0.93
r̄=0.93
Time (s)
g
fish 1
Neural Mode 4
Neural Mode 1
Neural Mode 2
h
fish 2
Neural Mode 4
Neural Mode 1
Neural Mode 2
d
mode 1
mode 2
mode 3
mode 4
mode 5
Correlation Across Trials
f
mode 1
mode 2
mode 3
mode 4
mode 5
Correlation to Average
i
average
Neural Mode 4
Neural Mode 1
Neural Mode 2

Figure 2. Latent dynamics in the optic tecta of zebrafish larvae in response to visual stimulation.
a. *Illustration of our approach to data analysis. Datasets such as the one shown on the left consisted of fluorescence traces from n neurons. These were trial averaged and the dimensionality of the trial averaged data was reduced using PCA. The new k dimensions are referred to as neural modes.*
b. *The first 5 neural modes explain ~90% of the variance in the data. The shaded area represents the standard deviation, n=9).*
c. *Shown are the latent dynamics of an individual wild type larva for the first 5 neural modes. The latent dynamics were calculated independently for each of the three trials. The mean correlation of the dynamics among the individual trials to the trial average is shown as $\bar{r}$. The presentation of each stimulus is shown as a gray bar, and the direction of each stimulus is shown at the top.*
d. *Graph summarizing the mean correlations across trials along each mode for the wild type larvae (0.98±0.006, mode 1; 0.94±0.012, mode 2; 0.96±0.01, mode 3; 0.95±0.017, mode 4; 0.94±0.032, mode 5 ;n=9)*
e. *Latent dynamics determined from trial averaged data. Traces (purple) are the dynamics from individual larvae and the shaded area (blue) is the variance for the wild type group. The value, $\bar{r}$, represents the mean correlation of each individual neural mode to the mean dynamics averaged across the group (see **f**).*
f. *Summary of the correlation between individual larvae and the group average along neural modes (0.97±0.008, mode 1; 0.93±0.014, mode 2; 0.91±0.017, mode 3; 0.93±0.015, mode 4; 0.93±0.013, mode 5; n=9).*
g,h. *Three-dimensional representation of latent dynamics for two, individual larvae. Each color represents a direction of motion for the visual stimulus. The excursions of neural trajectories during stimulus presentation describes a roughly circular neural manifold.*
i. *A three-dimensional representation of latent dynamics averaged across the wild type group (n=9).*

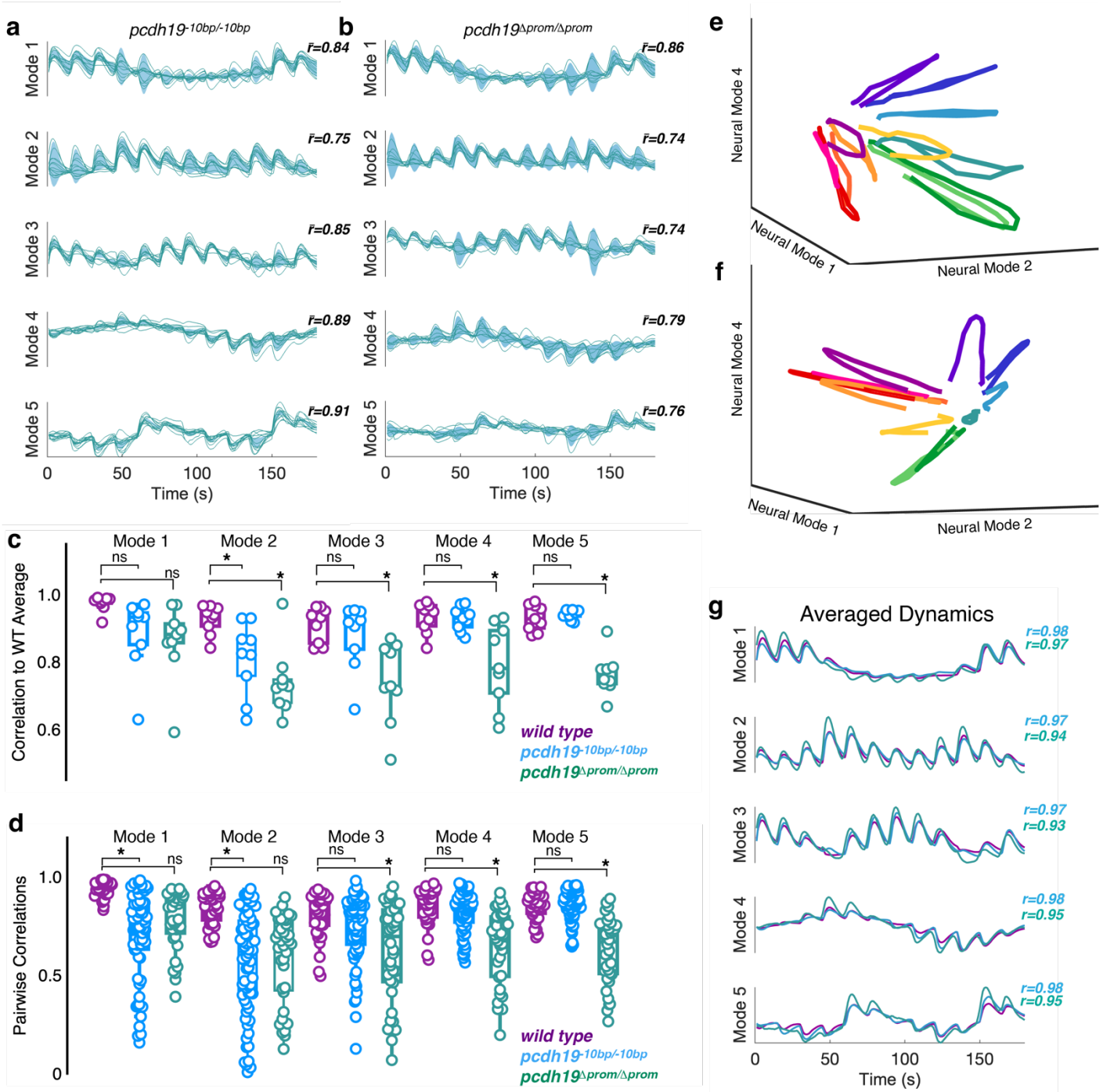
a
pcdh19-10bp/-10bp
Mode 1
Mode 2
Mode 3
Mode 4
Mode 5
r̄=0.84
r̄=0.75
r̄=0.85
r̄=0.89
r̄=0.91
0
50
100
150
Time (s)
b
pcdh19Δprom/Δprom
r̄=0.86
r̄=0.74
r̄=0.74
r̄=0.79
r̄=0.76
e
Neural Mode 4
Neural Mode 1
Neural Mode 2
f
c
Correlation to WT Average
1.0
0.8
0.6
ns
*
wild type
pcdh19-10bp/-10bp
pcdh19Δprom/Δprom
d
Pairwise Correlations
0.5
0
g
Averaged Dynamics
r=0.98
r=0.97
r=0.97
r=0.94
r=0.97
r=0.93
r=0.98
r=0.95
r=0.98
r=0.95

Figure 3. Mutations in pcdh19 lead to altered neural dynamics.

a,b. *Shown are latent dynamics determined from trial averaged neural data collected in homozygous pcdh19^{-10bp}* (***a***) and *pcdh19$^{\Delta prom}$* (***b***) *mutant larvae. Individual traces are in teal and the shaded area in blue indicates the group variance. The value, $\bar{r}$, represents the mean correlation of each individual neural mode to the group averaged neural mode. We obtained a total of 3589 visually responsive neurons from pcdh19^{-10bp} larvae, and 2172 neurons from pcdh19$^{\Delta prom}$ larvae.*

c. *Boxplot shows the correlation of individual trial-averaged neural modes to the wild type average (wild type, n=9: 0.97±0.008, mode 1; 0.93±0.014, mode 2; 0.91±0.017, mode 3; 0.93±0.015, mode 4; 0.93±0.013, mode 5; pcdh19^{-10bp}, n=12: 0.84±0.035, mode 1; 0.75±0.03, mode 2; 0.85±0.027, mode 3; 0.89±0.014, mode 4; 0.91±0.015, mode 5; pcdh19$^{\Delta prom}$, n=9: 0.88±0.03, mode 1; 0.78±0.04, mode 2; 0.77±0.046, mode 3; 0.80±0.04, mode 4; 0.78±0.022, mode 5; *p<0.05, Dunnett's test).*

d. *Pairwise within-group correlations of neural modes for each genotype (wild type,n=36: 0.94±0.013, mode 1; 0.84±0.028, mode 2; 0.81±0.038, mode 3; 0.85±0.031, mode 4; 0.85±0.023, mode 5; pcdh19^{-10bp}, n=66: 0.71±0.064, mode 1; 0.56±0.076, mode 2; 074±0.051, mode 3; 0.82±0.03, mode 4; 0.86±0.022, mode 5 ; pcdh19$^{\Delta prom}$, n=36: 0.78±0.05, mode 1; 0.59±0.075, mode 2; 0.61±0.095, mode 3; 0.64±0.031, mode 4; 0.63±0.056, mode 5; *p<0.05, Dunnett's test).*

e,f. *Three-dimensional representations of latent dynamics of individual pcdh19$^{\Delta prom}$ mutant larvae. The view is the same as in* ***Fig. 2g-i****.*

g. *Neural modes were averaged within each genotype (wild type/purple, pcdh19^{-10bp}/blue, pcdh19$^{\Delta prom}$/teal. The value, r, represents the correlation of each mutant average with the wild type average (pcdh19^{-10bp}/blue, pcdh19$^{\Delta prom}$/teal).*

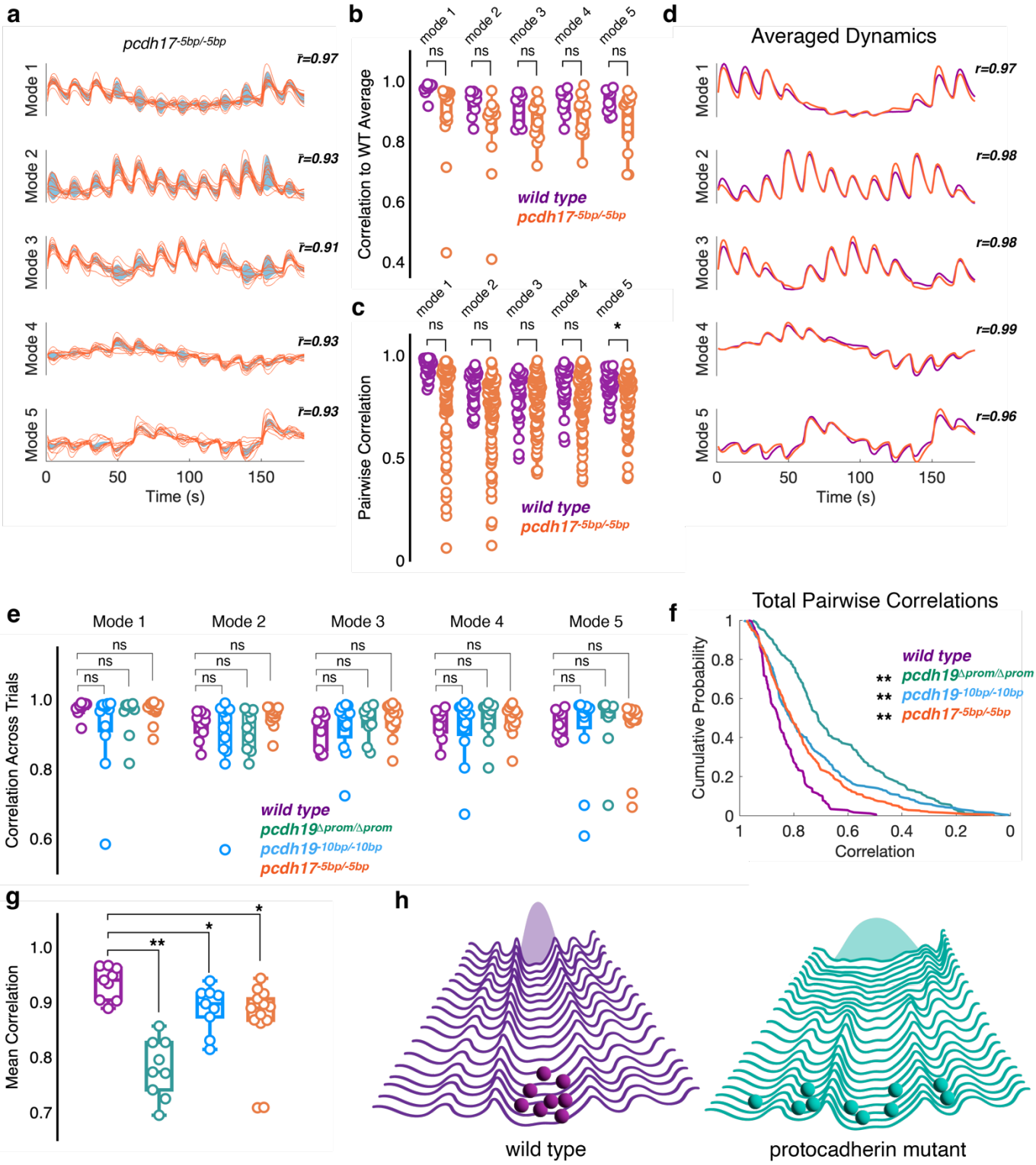
a
pcdh17-5bp/-5bp
Mode 1
Mode 2
Mode 3
Mode 4
Mode 5
r̄=0.97
r̄=0.93
r̄=0.91
r̄=0.93
r̄=0.93
0
50
100
150
Time (s)
b
mode 1
mode 2
mode 3
mode 4
mode 5
ns
Correlation to WT Average
1.0
0.8
0.6
0.4
wild type
pcdh17-5bp/-5bp
c
Pairwise Correlation
1.0
0.5
0
*
d
Averaged Dynamics
r=0.97
r=0.98
r=0.98
r=0.99
r=0.96
e
Correlation Across Trials
1.0
0.8
0.6
wild type
pcdh19Δprom/Δprom
pcdh19-10bp/-10bp
pcdh17-5bp/-5bp
f
Total Pairwise Correlations
Cumulative Probability
Correlation
**
g
Mean Correlation
1.0
0.9
0.8
0.7
h
wild type
protocadherin mutant

Figure 4. Mutations in pcdh17 lead to altered neural dynamics.

a. *Latent dynamics computed from trial averaged neural data collected in homozygous pcdh17^{-5bp} mutant larvae. Individual traces are in orange and the shaded area in blue indicates the group variance. The value, $\bar{r}$, represents the mean correlation of each individual neural mode to the group average of that neural mode. We obtained a total of 3561 visually-responsive neurons.*

b. *The correlation of individual trial-averaged neural modes to the wild type average (wild type: 0.97±0.008, mode 1; 0.93±0.014, mode 2; 0.91±0.017, mode 3; 0.93±0.015, mode 4; 0.93±0.013, mode 5, n=9; pcdh17^{-5bp}: 0.87±0.042, mode 1; 0.83±0.04, mode 2; 0.87±0.019, mode 3; 0.89±0.027, mode 4; 0.87±0.093, mode 5, n=13).*

c. *Pairwise within-group correlations of neural modes for wild type (purple) and pcdh17 mutants (orange). (wild type, n=36: 0.94±0.013, mode 1; 0.84±0.028, mode 2; 0.81±0.038, mode 3; 0.85±0.031, mode 4; 0.85±0.023, mode 5; pcdh17^{-5bp}, n=78: 0.78±0.055, mode 1; 0.71±0.053, mode 2; 0.77±0.037, mode 3; 0.79±0.039, mode 4; 0.79±0.035, mode 5; *p,0.05, Dunnett's test).*

d. *Neural modes were averaged for pcdh17^{-5bp} mutants (orange) and the average was compared to the wild type average (purple). The value, $\bar{r}$, represents the correlation of each mutant average with the wild type average.*

e. *The mean trial to trial correlations are shown for wild type (purple), pcdh19^{-10bp} (blue) pcdh19$^{\Delta prom}$ (teal), and pcdh17^{-5bp} (orange) mutants. Trial-to-trial variability in the mutants is not statistically different from wild type larvae (wild type, n=9: 0.98±0.006, mode 1; 0.94±0.012, mode 2; 0.96±0.01, mode 3; 0.95±0.017, mode 4; 0.94±0.032, mode 5; pcdh19^{-10bp}: 0.92±0.034, mode 1; 0.89±0.034, mode 2; 0.92±0.022, mode 3; 0.92±0.027, mode 4; 0.91±0.036, mode 5; pcdh19$^{\Delta prom}$: 0.91±0.024, mode 1; 0.90±0.025, mode 2; 0.90±0.025, mode 3; 0.90±0.015, mode 4; 0.85±0.049, mode 5; pcdh17^{-5bp}, n=13: 0.97±0.009, mode 1; 0.95±0.009, mode 2; 0.94±0.013, mode 3; 0.94±0.012, mode 4; 0.92±0.026, mode 5).*

f. *Cumulative probability histogram for the distribution of all pairwise within group r values for wild type (purple), pcdh19^{-10bp} (blue) pcdh19$^{\Delta prom}$ (teal), and pcdh17^{-5bp} (orange) mutants. (**p<0.0001, Dunn's test).*

g. *Mean correlation (r) of individual datasets to the wild type average, averaged across neural modes (wild type, n=9: 0.90±0.018; pcdh19^{-10bp}, n=12: 0.83±0.017; pcdh19$^{\Delta prom}$, n=9: 0.74±0.033; pcdh17^{-5bp}, n=13: 0.82±0.028;*p<0.05, **p<0.0001, Dunnett's test).*

h. *Hypothesized roles of Pcdh19 and Pcdh17 in canalyzing the assembly of visual circuits in the zebrafish optic tectum. In the wild type scenario (left/purple), development is canalized and the outcomes (circuit response to visual stimulation) is restricted, showing a small distribution in outcomes (shaded Gaussian). In the case of protocadherin mutants (right/teal), the developmental landscape is flattened, allowing development to stochastically explore a variety of alternative paths, leading to an increased variation among outcomes (broad shaded distribution).*

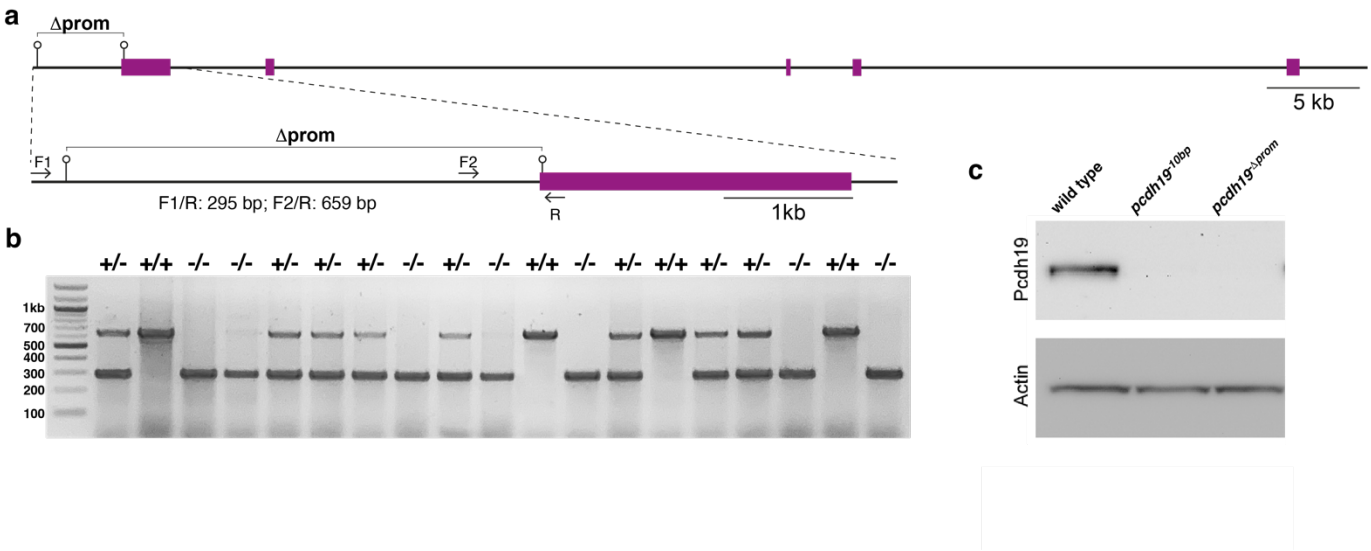

Supplemental Figure 1.

a *Schematic of the zebrafish pcdh19 gene, with exons shown in purple. Pins show the sites of CRISPR/Cas9 target sites. Primers used for PCR-based screening are shown, as are the expected sizes of the PCR products.*

b *Genotyping of mutant in-crosses using F1, F2 and R primers, which distinguish wild type, heterozygous and homozygous mutant larvae.*

C *Western blot showing the absence of Pcdh19 protein in both our previously published mutant line and in the promoterless line presented here.*

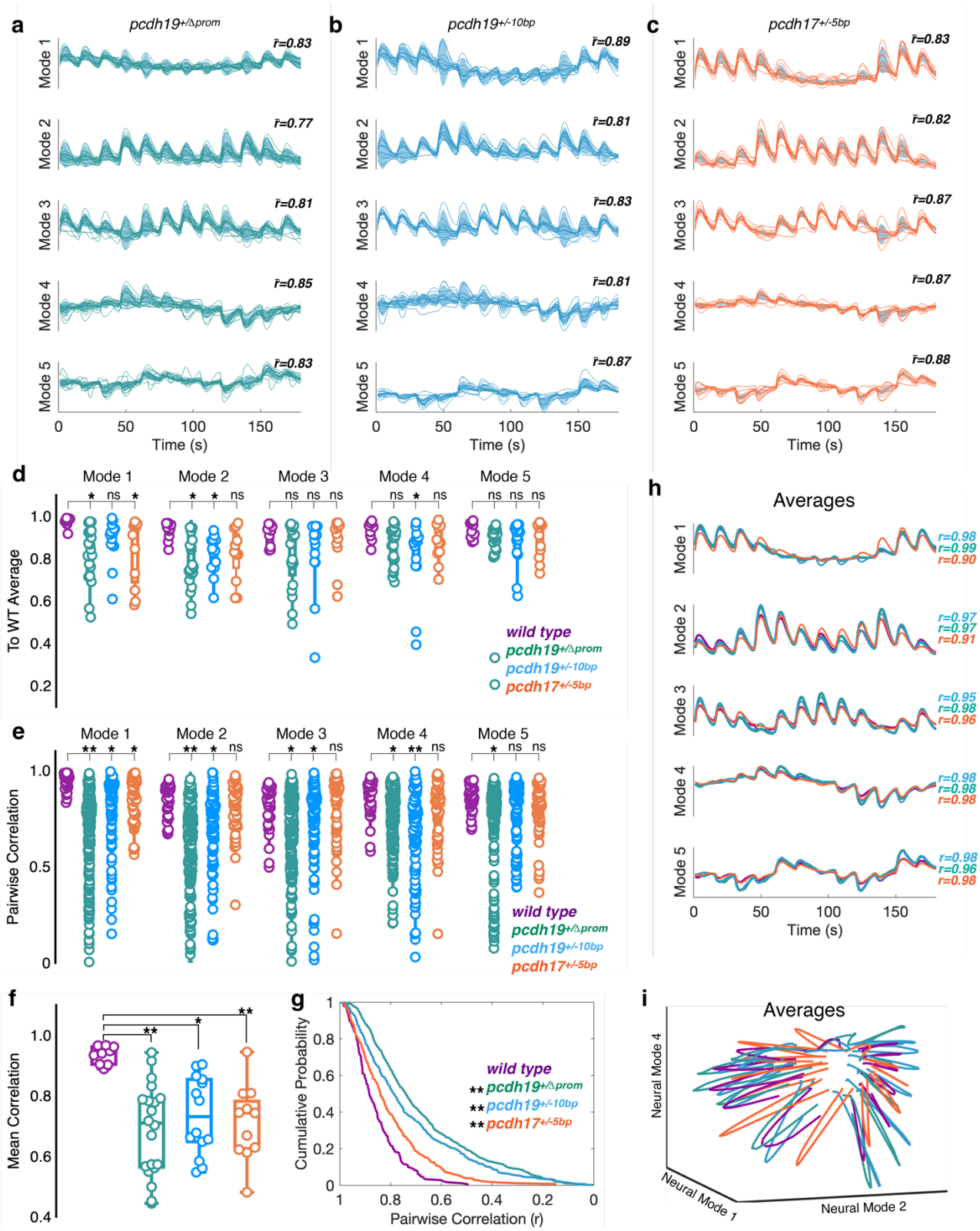
a
pcdh19+/Δprom
Mode 1
r̄=0.83
Mode 2
r̄=0.77
Mode 3
r̄=0.81
Mode 4
r̄=0.85
Mode 5
r̄=0.83
Time (s)
b
pcdh19+/-10bp
r̄=0.89
r̄=0.81
r̄=0.83
r̄=0.81
r̄=0.87
c
pcdh17+/-5bp
r̄=0.83
r̄=0.82
r̄=0.87
r̄=0.87
r̄=0.88
d
To WT Average
wild type
pcdh19+/Δprom
pcdh19+/-10bp
pcdh17+/-5bp
e
Pairwise Correlation
h
Averages
r=0.98
r=0.99
r=0.90
r=0.97
r=0.97
r=0.91
r=0.95
r=0.98
r=0.96
r=0.98
r=0.98
r=0.98
r=0.98
r=0.96
r=0.98
f
Mean Correlation
g
Cumulative Probability
Pairwise Correlation (r)
i
Averages
Neural Mode 4
Neural Mode 1
Neural Mode 2

Supplemental Figure 2. Heterozygous δ2-pcdh mutants exhibit altered neural dynamics.

a-c. *Latent dynamics computed from trial averaged neural data collected in heterozygous (**a**) pcdh19$^{\Delta prom}$, (**b**) pcdh19^{-10bp} and (**c**) pcdh17^{-5bp} mutant larvae. Individual traces are shown on top of the group variance, shaded in blue. The value, $\bar{r}$, represents the mean correlation of each individual neural mode to the wild type average of that neural mode.*

d. *The correlation of individual trial-averaged neural modes to the wild type average (wild type: 0.97±0.008, mode 1; 0.93±0.014, mode 2; 0.91±0.017, mode 3; 0.93±0.015, mode 4; 0.93±0.013, mode 5, n=9; pcdh19$^{\Delta prom}$: 0.82±0.029, mode 1; 0.77±0.026, mode 2; 0.81±0.033, mode 3; 0.85±0.02, mode 4; 0.83±0.044, mode 5, n=20; pcdh19^{-10bp} : 0.89±0.027, mode 1; 0.81±0.24, mode 2; 0.83±0.047, mode 3; 0.81±0.047, mode 4; 0.87±0.029, mode 5, n=14; pcdh17^{-5bp}: 0.83±0.048, mode 1; 0.82±0.038, mode 2; 0.87±0.036, mode 3; 0.87±0.027, mode 4; 0.88±0.026, mode 5, n=11). (*p<0.05, Dunnett's test).*

e. *Pairwise within-group correlations of neural modes for wild type (purple) and pcdh17 mutants (orange). (wild type, n=36: 0.94±0.007, mode 1; 0.84±0.014, mode 2; 0.81±0.019, mode 3; 0.85±0.016, mode 4; 0.85±0.011, mode 5; pcdh19$^{\Delta prom}$, n=190: 0.66±0.017, mode 1; 0.60±0.016, mode 2; 0.66±0.015, mode 3; 0.74±0.012, mode 4; 0.73±0.016, mode 5 pcdh19^{-10bp} , n=91: 0.8±0.02, mode 1; 0.68±0.022, mode 2; 0.72±0.024, mode 3; 0.65±0.026, mode 4; 0.78±0.017, mode 5; pcdh17^{-5bp}, n=55: 0.84±0.016, mode 1; 080±0.017, mode 2; 0.81±0.0223, mode 3; 0.79±0.022, mode 4; 0.79±0.018, mode 5; **p<0.0001, *p,0.05, Dunnett's test).*

f. *Neural modes were averaged for wild type (purple, 0.9±0.018), pcdh19^{-10bp} (blue, 0.74±0.034), pcdh19$^{\Delta prom}$ (teal, 0.69±0.041) and pcdh17^{-5bp} mutants (orange, 0.71±0.038) and the average was compared to the wild type average (purple). (**p<0.0001, *p<0.05, Dunnett's test).*

g. *Cumulative probability histogram for the distribution of all pairwise within group r values for wild type (purple), pcdh19^{-10bp} (blue) pcdh19$^{\Delta prom}$ (teal), and pcdh17^{-5bp} (orange) mutants. (**p<0.0001, Dunn's test).*

h. *Mean correlation (r) of individual datasets to the wild type average, averaged across neural modes (wild type, n=9: 0.90±0.018; pcdh19^{-10bp}, n=12: 0.83±0.017; pcdh19$^{\Delta prom}$, n=9: 0.74±0.033; pcdh17^{-5bp}, n=13: 0.82±0.028;*p<0.05, **p<0.0001, Dunnett's test).*

i. *Plotting of averaged dynamics along neural modes 1, 2 and 4 for wild type (purple), pcdh19^{-10bp} (blue) pcdh19$^{\Delta prom}$ (teal), and pcdh17^{-5bp} (orange) heterozygous mutants.*

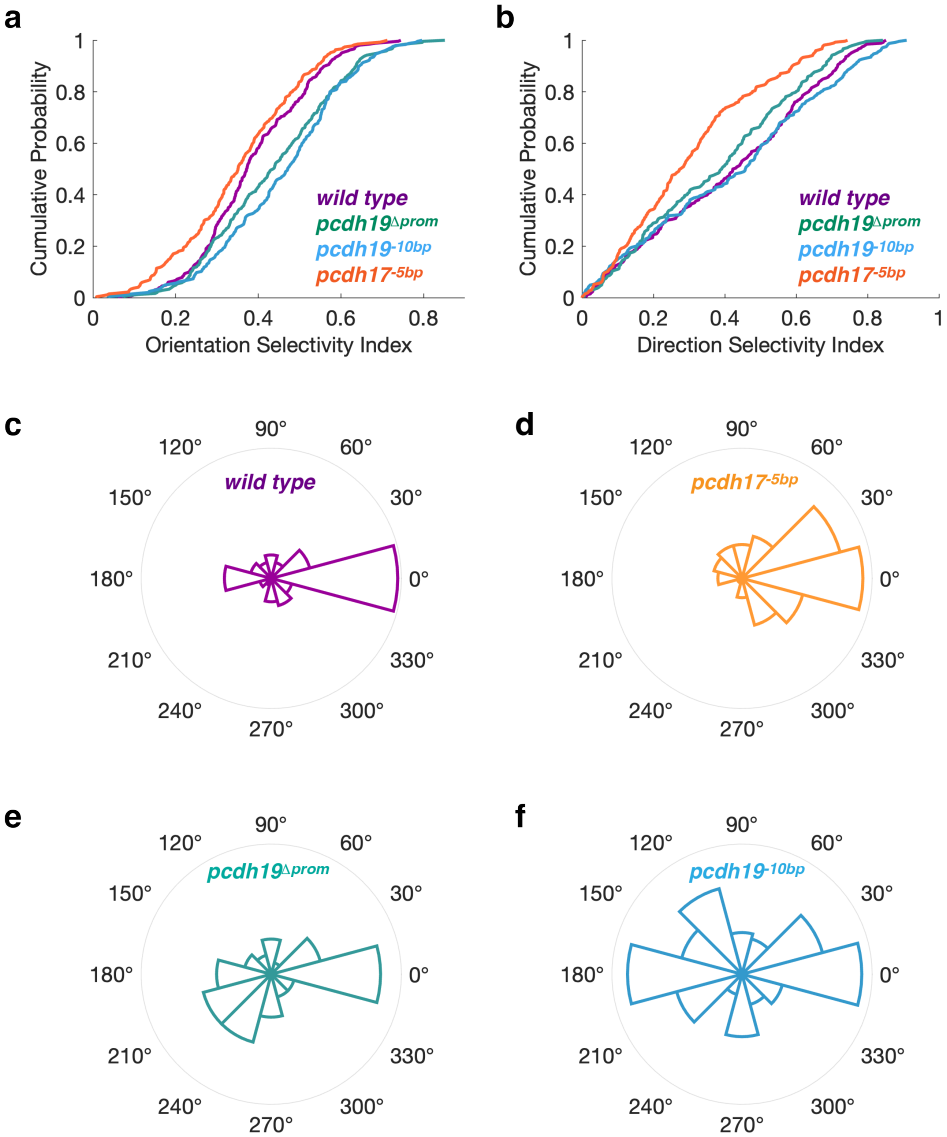

Supplemental Figure 3. Altered orientation selectivity and direction selectivity in δ2-pcdh mutants.

a. *Cumulative probability distributions of orientation selectivity for all neurons in wild type (purple), pcdh19^{-10bp} (blue) pcdh19$^{\Delta prom}$ (teal), and pcdh17^{-5bp} (orange) mutants. Pcdh17 and Pcdh19 mutants exhibit distinct effects on orientation selectivity, with pcdh17^{-5bp} mutants exhibiting an overall shift toward reduced orientation selectivity, and both pcdh19^{-10bp} and pcdh19$^{\Delta prom}$ showing a shift toward increased direction selectivity.(**p<0.0001; Dunn's test).* ***b.*** *Cumulative probability distributions of direction selectivity for all neurons in wild type (purple), pcdh19^{-10bp} (blue) pcdh19$^{\Delta prom}$ (teal), and pcdh17^{-5bp} (orange) mutants. The pcdh17^{-5bp} mutants exhibit a dramatic shift toward reduced direction selectivity. In contrastboth pcdh19^{-10bp} and pcdh19$^{\Delta prom}$ showing a shift toward increased direction selectivity.(*p<0.05, **p<0.0001; Dunn's test).*

c. *A polar histogram showing the preferred directions of direction selective neurons (DSI>0.33) in wild type larvae. The preferred direction as obtained as the vector average of the responses across all stimuli.*

662 ***d.*** *A polar histogram showing the preferred direction of direction selective neurons in pcdh17^{-5bp} mutants.*
663 *There is an increase in the number of cells that prefer caudal-to-rostral motion (p<0.0001; Watson's U2*
664 *test).*
665 ***e.*** *A polar histogram showing the preferred direction of direction selective neurons in pcdh19$^{\Delta prom}$*
666 *mutants. There is a slight decrease in cells responsive to caudal-to-rostral motion and an increase in the*
667 *number of cells that prefer motion between 195º-240º (p<0.0001; Watson's U2 test).*
668 ***f.*** *A polar histogram showing the preferred direction of direction selective neurons in pcdh19^{-10bp}*
669 *mutants. There is a large increase in the proportion of cells responsive to directions other than caudal-*
670 *to-rostral motion, particularly directions centered around 120º and 180º (p<0.0001; Watson's U2 test).*
671
672
673
674
675
676
677
678
679
680
681
682
683
684
685
686
687
688
689 **REFERENCES**
690

691 1. Waddington, C. (1942). Canalization of development and the inheritance of acquired characters. Nature
692 *150*, 563–565. https://doi.org/10.1007/s00128-015-1540-6.

693 2. Xu, T., Nenning, K.-H., Schwartz, E., Hong, S.-J., Vogelstein, J.T., Goulas, A., Fair, D.A., Schroeder,
694 C.E., Margulies, D.S., Smallwood, J., et al. (2020). Cross-species functional alignment reveals
695 evolutionary hierarchy within the connectome. NeuroImage *223*, 117346.
696 https://doi.org/10.1016/j.neuroimage.2020.117346.

697 3. Mars, R.B., Sotiropoulos, S.N., Passingham, R.E., Sallet, J., Verhagen, L., Khrapitchev, A.A., Sibson,
698 N., and Jbabdi, S. (2018). Whole brain comparative anatomy using connectivity blueprints. eLife *7*,
699 e35237. https://doi.org/10.7554/elife.35237.

700 4. Kitano, H. (2004). Biological robustness. Nature reviews Genetics *5*, 826–837.
701 https://doi.org/10.1038/nrg1471.

702 5. Masel, J., and Siegal, M.L. (2009). Robustness: mechanisms and consequences. Trends Genet. *25*, 395–
703 403. https://doi.org/10.1016/j.tig.2009.07.005.

704 6. Geschwind, D.H., and Levitt, P. (2007). Autism spectrum disorders: developmental disconnection
705 syndromes. Current opinion in neurobiology *17*, 103–111. https://doi.org/10.1016/j.conb.2007.01.009.

706 7. Yamasaki, T., Maekawa, T., Fujita, T., and Tobimatsu, S. (2017). Connectopathy in Autism Spectrum
707 Disorders: A Review of Evidence from Visual Evoked Potentials and Diffusion Magnetic Resonance
708 Imaging. Frontiers in neuroscience *11*, 158–14. https://doi.org/10.3389/fnins.2017.00627.

709 8. Lynall, M.-E., Bassett, D.S., Kerwin, R., McKenna, P.J., Kitzbichler, M., Müller, U., and Bullmore, E.
710 (2010). Functional connectivity and brain networks in schizophrenia. Journal of Neuroscience *30*, 9477–
711 9487. https://doi.org/10.1523/jneurosci.0333-10.2010.

712 9. Friston, K., Brown, H.R., Siemerkus, J., and Stephan, K.E. (2016). The dysconnection hypothesis
713 (2016). Schizophrenia Research *176*, 83–94. https://doi.org/10.1016/j.schres.2016.07.014.

714 10. Belmonte, M.K., Allen, G., Beckel-Mitchener, A., Boulanger, L.M., Carper, R.A., and Webb, S.J.
715 (2004). Autism and abnormal development of brain connectivity. Journal of Neuroscience *24*, 9228–9231.
716 https://doi.org/10.1523/jneurosci.3340-04.2004.

717 11. Woodbury-Smith, M., Nicolson, R., Zarrei, M., Yuen, R.K.C., Walker, S., Howe, J., Uddin, M.,
718 Hoang, N., Buchanan, J.A., Chrysler, C., et al. (2017). Variable phenotype expression in a family
719 segregating microdeletions of the NRXN1 and MBD5 autism spectrum disorder susceptibility genes. npj
720 Genom. Med. *2*, 17. https://doi.org/10.1038/s41525-017-0020-9.

721 12. Masfrand, S. de, Cogné, B., Nizon, M., Deb, W., Goldenberg, A., Lecoquierre, F., Nicolas, G.,
722 Bournez, M., Vitobello, A., Mau-Them, F.T., et al. (2024). Penetrance, variable expressivity and
723 monogenic neurodevelopmental disorders. Eur. J. Méd. Genet. *69*, 104932.
724 https://doi.org/10.1016/j.ejmg.2024.104932.

725 13. Chien, Y., Wu, C., and Tsai, H. (2021). The Comorbidity of Schizophrenia Spectrum and Mood
726 Disorders in Autism Spectrum Disorder. Autism Res. *14*, 571–581. https://doi.org/10.1002/aur.2451.

727 14. Cristino, A.S., Williams, S.M., Hawi, Z., An, J.-Y., Bellgrove, M.A., Schwartz, C.E., Costa, L. da F.,
728 and Claudianos, C. (2013). Neurodevelopmental and neuropsychiatric disorders represent an
729 interconnected molecular system. Molecular psychiatry *19*, 294–301. https://doi.org/10.1038/mp.2013.16.

730 15. Hamlyn, J., Duhig, M., McGrath, J., and Scott, J. (2013). Modifiable risk factors for schizophrenia
731 and autism - Shared risk factors impacting on brain development. Neurobiology of disease *53*, 3–9.
732 https://doi.org/10.1016/j.nbd.2012.10.023.

733 16. Zhu, X., Need, A.C., Petrovski, S., and Goldstein, D.B. (2014). One gene, many neuropsychiatric
734 disorders: lessons from Mendelian diseases. Nature Publishing Group *17*, 773–781.
735 https://doi.org/10.1038/nn.3713.

736 17. Hulpiau, P., and Roy, F.V. (2009). Molecular evolution of the cadherin superfamily. The international
737 journal of biochemistry & cell biology *41*, 349–369. https://doi.org/10.1016/j.biocel.2008.09.027.

738 18. Nollet, F., Kools, P., and Roy, F. van (2000). Phylogenetic analysis of the cadherin superfamily
739 allows identification of six major subfamilies besides several solitary members. Journal of Molecular
740 Biology *299*, 551–572. https://doi.org/10.1006/jmbi.2000.3777.

19. Jontes, J.D. (2017). The Cadherin Superfamily in Neural Circuit Assembly. Cold Spring Harbor perspectives in biology *10*, a029306. https://doi.org/10.1101/cshperspect.a029306.

20. Piton, A., Gauthier, J., Hamdan, F.F., Lafrenière, R.G., Yang, Y., Henrion, E., Laurent, S., Noreau, A., Thibodeau, P., Karemera, L., et al. (2011). Systematic resequencing of X-chromosome synaptic genes in autism spectrum disorder and schizophrenia. Molecular psychiatry *16*, 867–880. https://doi.org/10.1038/mp.2010.54.

21. Vlaskamp, D.R.M., Bassett, A.S., Sullivan, J.E., Robblee, J., Sadleir, L.G., Scheffer, I.E., and Andrade, D.M. (2019). Schizophrenia is a later-onset feature of PCDH19Girls Clustering Epilepsy. Epilepsia *60*, 429–440. https://doi.org/10.1111/epi.14678.

22. Dibbens, L.M., Tarpey, P.S., Hynes, K., Bayly, M.A., Scheffer, I.E., Smith, R., Bomar, J., Sutton, E., Vandeleur, L., Shoubridge, C., et al. (2008). X-linked protocadherin 19 mutations cause female-limited epilepsy and cognitive impairment. Nature Genetics *40*, 776–781. https://doi.org/10.1038/ng.149.

23. Depienne, C., Depienne, C., Bouteiller, D., Bouteiller, D., Keren, B., Keren, B., Cheuret, E., Cheuret, E., Poirier, K., Poirier, K., et al. (2009). Sporadic Infantile Epileptic Encephalopathy Caused by Mutations in PCDH19 Resembles Dravet Syndrome but Mainly Affects Females. PLoS Genetics *5*, e1000381. https://doi.org/10.1371/journal.pgen.1000381.t001.

24. Bollmann, J.H., and Engert, F. (2009). Subcellular Topography of Visually Driven Dendritic Activity in the Vertebrate Visual System. Neuron *61*, 895–905. https://doi.org/10.1016/j.neuron.2009.01.018.

25. Niell, C.M., and Smith, S.J. (2005). Functional imaging reveals rapid development of visual response properties in the zebrafish tectum. Neuron *45*, 941–951. https://doi.org/10.1016/j.neuron.2005.01.047.

26. Baier, H., and Scott, E.K. (2024). The Visual Systems of Zebrafish. Annu. Rev. Neurosci. *47*, 255–276. https://doi.org/10.1146/annurev-neuro-111020-104854.

27. Förster, D., Helmbrecht, T.O., Mearns, D.S., Jordan, L., Mokayes, N., and Baier, H. (2020). Retinotectal circuitry of larval zebrafish is adapted to detection and pursuit of prey. Elife *9*, e58596. https://doi.org/10.7554/elife.58596.

28. Giovannucci, A., Friedrich, J., Gunn, P., Kalfon, J., Brown, B.L., Koay, S.A., Taxidis, J., Najafi, F., Gauthier, J.L., Zhou, P., et al. (2019). CaImAn an open source tool for scalable calcium imaging data analysis. eLife *8*, e38173. https://doi.org/10.7554/elife.38173.

29. Vyas, S., Golub, M.D., Sussillo, D., and Shenoy, K.V. (2020). Computation Through Neural Population Dynamics. Annu Rev Neurosci *43*, 249–275. https://doi.org/10.1146/annurev-neuro-092619-094115.

30. Saxena, S., and Cunningham, J.P. (2019). Towards the neural population doctrine. Curr. Opin. Neurobiol. *55*, 103–111. https://doi.org/10.1016/j.conb.2019.02.002.

31. Langdon, C., Genkin, M., and Engel, T.A. (2023). A unifying perspective on neural manifolds and circuits for cognition. Nat. Rev. Neurosci. *24*, 363–377. https://doi.org/10.1038/s41583-023-00693-x.

32. Sadtler, P.T., Quick, K.M., Golub, M.D., Chase, S.M., Ryu, S.I., Tyler-Kabara, E.C., Yu, B.M., and Batista, A.P. (2014). Neural constraints on learning. Nature *512*, 423–426. https://doi.org/10.1038/nature13665.

33. Gallego, J.A., Perich, M.G., Miller, L.E., and Solla, S.A. (2017). Neural Manifolds for the Control of Movement. Neuron *94*, 978–984. https://doi.org/10.1016/j.neuron.2017.05.025.

34. Safaie, M., Chang, J.C., Park, J., Miller, L.E., Dudman, J.T., Perich, M.G., and Gallego, J.A. (2023). Preserved neural dynamics across animals performing similar behaviour. Nature *623*, 765–771. https://doi.org/10.1038/s41586-023-06714-0.

35. Gallego, J.A., Perich, M.G., Chowdhury, R.H., Solla, S.A., and Miller, L.E. (2020). Long-term stability of cortical population dynamics underlying consistent behavior. Nat. Neurosci. *23*, 260–270. https://doi.org/10.1038/s41593-019-0555-4.

36. Cooper, S.R., Emond, M.R., Duy, P.Q., Liebau, B.G., Wolman, M.A., and Jontes, J.D. (2015). Protocadherins control the modular assembly of neuronal columns in the zebrafish optic tectum. J Cell Biol *211*, 807–814. https://doi.org/10.1083/jcb.201507108.

37. Biswas, S., Emond, M.R., Chenoweth, K.P., and Jontes, J.D. (2021). δ-Protocadherins regulate neural progenitor cell division by antagonizing Ryk and Wnt/β-catenin signaling. Iscience *24*, 102932. https://doi.org/10.1016/j.isci.2021.102932.

38. El-Brolosy, M.A., Kontarakis, Z., Rossi, A., Kuenne, C., Günther, S., Fukuda, N., Kikhi, K., Boezio, G.L.M., Takacs, C.M., Lai, S.-L., et al. (2019). Genetic compensation triggered by mutant mRNA degradation. Nature *568*, 193–197. https://doi.org/10.1038/s41586-019-1064-z.

39. Rossi, A., Kontarakis, Z., Gerri, C., Nolte, H., Hölper, S., Krüger, M., and Stainier, D.Y.R. (2015). Genetic compensation induced by deleterious mutations but not gene knockdowns. Nature *524*, 230–233. https://doi.org/10.1038/nature14580.

40. Redies, C., Hertel, N., and Hübner, C.A. (2012). Cadherins and neuropsychiatric disorders. Brain research *1470*, 130–144. https://doi.org/10.1016/j.brainres.2012.06.020.

41. Hirano, S., and Takeichi, M. (2012). Cadherins in Brain Morphogenesis and Wiring. Physiological reviews *92*, 597–634. https://doi.org/10.1152/physrev.00014.2011.

42. Tsai, N.-P., Wilkerson, J.R., Guo, W., Maksimova, M.A., Demartino, G.N., Cowan, C.W., and Huber, K.M. (2012). Multiple Autism-Linked Genes Mediate Synapse Elimination via Proteasomal Degradation of a Synaptic Scaffold PSD-95. Cell *151*, 1581–1594. https://doi.org/10.1016/j.cell.2012.11.040.

43. Morrow, E.M., Morrow, E.M., Yoo, S.-Y., Yoo, S.-Y., Flavell, S.W., Flavell, S.W., Kim, T.-K., Kim, T.-K., Lin, Y., Lin, Y., et al. (2008). Identifying autism loci and genes by tracing recent shared ancestry. Science (New York, NY) *321*, 218–223. https://doi.org/10.1126/science.1157657.

44. Kasnauskiene, J., Kasnauskiene, J., Ciuladaite, Z., Ciuladaite, Z., Preiksaitiene, E., Preiksaitiene, E., Matulevičienė, A., Matulevičienė, A., Alexandrou, A., Alexandrou, A., et al. (2012). A single gene

811 deletion on 4q28.3: PCDH18 - A new candidate gene for intellectual disability? European Journal of
812 Medical Genetics *55*, 1–4. https://doi.org/10.1016/j.ejmg.2012.02.010.

813 45. Chang, H., Hoshina, N., Zhang, C., Ma, Y., Cao, H., Wang, Y., Wu, D., Bergen, S.E., n, M.L. eacute,
814 Hultman, C.M., et al. (2017). The protocadherin 17 gene affects cognition, personality, amygdala
815 structure and function, synapse development and risk of major mood disorders. Molecular psychiatry *23*,
816 1–13. https://doi.org/10.1038/mp.2016.231.

817 46. Light, S.E.W., and Jontes, J.D. (2019). Multiplane calcium imaging reveals disrupted development of
818 network topology in zebrafish pcdh19 mutants. Eneuro *6*, ENEURO.0420-18.2019.
819 https://doi.org/10.1523/eneuro.0420-18.2019.

820 47. Giansante, G., Mazzoleni, S., Zippo, A.G., Ponzoni, L., Ghilardi, A., Maiellano, G., Lewerissa, E.,
821 Hugte, E. van, Kasri, N.N., Francolini, M., et al. (2023). Neuronal network activity and connectivity are
822 impaired in a conditional knockout mouse model with PCDH19 mosaic expression. Mol Psychiatr, 1–16.
823 https://doi.org/10.1038/s41380-023-02022-1.

824 48. Robens, B.K., Yang, X., McGraw, C.M., Turner, L.H., Robens, C., Thyme, S., Rotenberg, A., and
825 Poduri, A. (2022). Mosaic and non-mosaic protocadherin 19 mutation leads to neuronal hyperexcitability
826 in zebrafish. Neurobiol Dis *169*, 105738–105738. https://doi.org/10.1016/j.nbd.2022.105738.

827 49. Hallgrimsson, B., Green, R.M., Katz, D.C., Fish, J.L., Bernier, F.P., Roseman, C.C., Young, N.M.,
828 Cheverud, J.M., and Marcucio, R.S. (2019). The developmental-genetics of canalization. Semin. Cell
829 Dev. Biol. *88*, 67–79. https://doi.org/10.1016/j.semcdb.2018.05.019.

830 50. Siegal, M.L., and Bergman, A. (2002). Waddington's canalization revisited: developmental stability
831 and evolution. Proceedings of the National Academy of Sciences of the United States of America *99*,
832 10528–10532. https://doi.org/10.1073/pnas.102303999.

833 51. Pologruto, T.A., Sabatini, B.L., and Svoboda, K. (2003). ScanImage: flexible software for operating
834 laser scanning microscopes. Biomedical engineering online *2*, 13. https://doi.org/10.1186/1475-925x-2-
835 13.

836 52. Romano, S.A., Pietri, T., Pérez-Schuster, V., Jouary, A., Haudrechy, M., and Sumbre, G. (2015).
837 Spontaneous Neuronal Network Dynamics Reveal Circuit's Functional Adaptations for Behavior. Neuron
838 *85*, 1070–1085. https://doi.org/10.1016/j.neuron.2015.01.027.

839 53. Avitan, L., Pujic, Z., Mölter, J., Poll, M.V.D., Sun, B., Teng, H., Amor, R., Scott, E.K., and Goodhill,
840 G.J. (2017). Spontaneous Activity in the Zebrafish Tectum Reorganizes over Development and Is
841 Influenced by Visual Experience. Current Biology *27*, 2407-2419.e4.
842 https://doi.org/10.1016/j.cub.2017.06.056.

843 54. Gabriel, J.P., Trivedi, C.A., Maurer, C.M., Ryu, S., and Bollmann, J.H. (2012). Layer-specific
844 targeting of direction-selective neurons in the zebrafish optic tectum. Neuron *76*, 1147–1160.
845 https://doi.org/10.1016/j.neuron.2012.12.003.

55. Pnevmatikakis, E.A., and Giovannucci, A. (2017). NoRMCorre: An online algorithm for piecewise rigid motion correction of calcium imaging data. Journal of neuroscience methods *291*, 83–94. https://doi.org/10.1016/j.jneumeth.2017.07.031.